A rationale for the influence of grain size on failure of magnesium alloy AZ31: An in situ X-ray microtomography study

S. H. Mohamadi Azghandi, M. Weiss, B. D. Arhatari, J. Adrien, E. Maire, M. R. Barnett

A rationale for the influence of grain size on failure of magnesium alloy AZ31:

an *in situ* X-ray microtomography study

S.H. Mohamadi Azghandi[1,*], M. Weiss[1], B. D. Arhatari [2,3], J. Adrien[4], E. Maire[4], M.R. Barnett[1]

[1] Institute for Frontier Materials, Deakin University, Geelong, VIC 3216, Australia
[2] ARC Centre of Excellence in Advanced Molecular Imaging, Department of Chemistry and Physics, La Trobe University, VIC 3086, Australia
[3] Australian Synchrotron, ANSTO, Clayton 3168, Australia
[4]Université de Lyon, Mateis, INSA Lyon, CNRS UMR 5510 Villeurbanne, France
[*]h.mohamadiazghandi@deakin.edu.au

Abstract

The present study employs *in situ* X-ray microtomography to characterize the impact of grain size on void nucleation, growth and linkage during tensile loading of magnesium alloy AZ31. It was found that the tensile failure strain increased almost threefold when the grain size was reduced from 60 to 3 μm. Grain refinement led to reduced twins and void volume fractions but did not impact markedly on the relationship between void number density and strain. Grain refinement led to a greater proportion of voids forming at particles but, because of the higher strain to failure and the relatively unchanged rate of void formation, the finer grained samples displayed higher void number densities at failure. Failure appears to be via a void sheeting like mechanism, which is triggered once a critical void volume fraction is attained. The lower rates of void growth in finer grained samples thus lead to higher strains to failure. The impact of grain size on void growth is the critical relationship that explains why fine grain magnesium alloys often tend to display higher tensile ductility.

Keywords: Magnesium alloys, Grain size, Void formation, Twinning, X-ray tomography

1. Introduction

Magnesium alloy plates frequently display higher specific bending strength and stiffness compared to steel and aluminium alloys. However, its low room-temperature formability can limit certain applications [1]. This is often ascribed to a limited number of easily activated slip systems [2]. In consequence, the improvement in ductility seen with grain refinement and texture weakening has been rationalized in terms of an increase in activated deformation modes [2-14]. Grain refinement is attractive from a practical viewpoint because it increases both ductility and strength [5-9, 15-23] and its benefit has been explained in terms of increased non-basal slip [24-26] and/or grain boundary sliding [10, 11, 27]. In a number of cases, the concomitant suppression of twinning activity has also been emphasized [28, 29]. For a complete understanding, it is necessary to ascertain how these deformation mechanism based arguments interact with the mechanisms of failure.

Magnesium alloys typically fail in a ductile manner. That is, in tension, voids are seen to nucleate, grow and coalesce to produce catastrophic parting of the material. Microstructure heterogeneities such as twin boundaries [28, 30-36], grain boundaries [33, 37, 38] and second-phase particles [30-32, 39-43] have been identified as locations for void nucleation. Void growth has been examined by Nemcko, Wilkinson and co-workers [33, 44-47] and, as would be expected, it is seen to be heavily influenced by the microstructure and by the particular deformation modes active in the adjacent material. So the general picture that emerges is that while the voids are seen to nucleate in magnesium alloys in microstructural locations typically associated with void formation, the inhomogeneity of plastic strain and variation of local stress that arises from the material's strong plastic anisotropy quite possibly influences void growth. In tension, the final failure has been ascribed in a number of cases to a 'void sheeting' type mechanism [28, 33, 48] whereby a shear band develops in a primary dispersion of voids and the flow localization that ensues accelerates void linkage. Secondary voids are also probably formed in the shear band. In any case, catastrophic parting of the specimen follows rapidly after the localization begins, leading frequently to fracture surfaces with large portions inclined at an angle to the loading direction.

It is not completely clear how this rationale should be applied to understand the strong beneficial impact of grain refinement on the tensile ductility of magnesium. In addition to the influence of grain size on

deformation mode activity noted above, we have recently seen that in alloy AZ31 [49] the grain size seems to impact on void size and also that void nucleation at second-phase particles is more prevalent for finer grain sizes. These findings were limited to void information gathered at the point of fracture and the present study was initiated to validate the findings using strain mapping, interrupted x-ray tomography and void characterization. The aim is to develop a more comprehensive understanding of how the grain size impacts on tensile ductility in magnesium alloy AZ31 and thereby on magnesium alloys in general.

2. Material and methods

2.1. Materials and their preparation

The as-received material was a 150mm-thick, commercial hot-rolled AZ31 alloy with an average grain size of 30 μm and a chemical composition (*wt%*) of 3.12Al-1.3Zn-0.36Mn (Mg the balance) [49]. 10mm-thick plates were cut from the as-received material and hot rolled at 300° C in 4 clock-rolling passes with a reduction in thickness of 33% in each pass, using a 2000 kN rolling mill. The material was subjected to 5 minutes heating between each pass. The produced 2mm-sheet was annealed at 230° C for 1 h, 300° C for 16 h, 400° C for 16 h, 450° C for 24 h, 500° C for 4 h and 500° C for 24 h in an argon atmosphere-controlled muffle furnace. This produced average grain sizes of 3, 7, 12, 22, 30 and 60 μm in combination with basal textures that had very similar maximum intensities of pole figures. The as-received material includes Al-Mn second-phase particle and is free of Al-Mg phases. The produced materials have second-phase particles with similar size and volume fractions. The relevant data is provided in the supplementary (Fig. S-1, the data of 3 and 60 μm are presented in [50]).

2.2. Microstructure analysis

Samples were ground with 1200 grit SiC paper followed by mechanical polishing with diamond paste from 9 to 6 to 3 μm and with a final polish using colloidal silica slurry. After this, the surfaces were etched in acetic picral solution (100 ml ethanol, 10 ml H_2O, 6 g picric acid, 5 ml acetic acid) for 5 to 15 seconds. The microstructure was evaluated using optical microscopy. The as-polished samples were

also examined by electron backscatter diffraction (EBSD) and energy dispersive X-ray spectroscopy (EDS) techniques to determine the average grain size, the crystallographic orientation and the type of second-phase particles. The Oxford HKL channel 5 software was employed to analyse the EBSD maps and the average grain size was measured on ~8000 grains, based on the linear intercept method [51]. To distinguish the grain boundaries, a critical misorientation angle of 15° was used. The crystallographic textures were determined from electron-backscattered diffraction maps of at least 8000 grains. In order to statistically investigate the particles, an area of approximately 2.5 mm^2 (about 1000 particles) was examined from each sample. In this examination, only particles that were larger than 1 μm were taken into account.

2.3. Mechanical testing

The sheet materials were machined into tensile specimens along the transversal direction (TD) with a gauge length of 25 mm based on ASTM-B557M [52]. The tensile testing was conducted with a 30 kN Instron machine equipped with a video extensometer at a strain rate of 1×10^{-3} s^{-1}. The GOM-ARAMIS system was employed to measure local strain (principal tensile strain) using digital image correlation (DIC).

2.4. In situ micro X-ray computed tomography

The formation of voids during tensile loading was studied using Xradia (microXCT-200) micro X-ray computed tomography (μXCT) that produced three dimensional image of a sample [53]. X-ray micrograph images were attained with a rotation increment of 0.5° for a 180° range, using a tungsten anode tube with a voltage of 50 kV and a power of 10 W. The magnification of the detector was 4X with 2×2 binning. The highest resolution obtained was a voxel size of 2.94 μm with a field of view of 2×2 mm and a total acquisition time of 1 h. The beam hardening correction and removal of spurious features (rings) as well as the 3D reconstruction of the x-ray micrograph were performed using the TXM Reconstructor software. The commercial (Avizo) software was used to carry out the geometrical void

analysis. A detectable feature is expected to have at least 3 voxels in each direction, X, Y, Z [33]. Thus, only voids with a volume larger than $27 \times (2.94)^3 = 686\ \mu m^3$ were reliably detected.

In situ μXCT tensile testing was conducted using a 500 N Deben stage tensile rig at a constant speed of 3 μm/s (corresponding to a strain rate of 3×10^{-3} s^{-1}). The μXCT tensile specimens having the gauge length of 1 mm (as shown in [33]) were cut along the TD by electrical-discharge machining. A volume of 0.5 mm^3 in the centre of the gauge region was examined by X-ray microtomography. The Local true strain is calculated by

$$\varepsilon = ln\frac{A_0}{A} \qquad \text{Equation 1}$$

where A_0 ($A_0 = t_0 \times w_0$) and A ($A = t \times w$) are the initial and the current cross-sectional area of the specimen as a function of the thickness and width. Fractured samples were also examined using high-resolution EasytomNano μXCT (Rx Solutions) with a voxel size of 1 μm. In this latter case, only voids that were larger than 27 agglomerated voxels, i.e. $27 \times (1)^3 = 27\mu m^3$ in volume, were kept for the analysis. The Hammamatsu X-ray source was operated with a LaB_6 cathode at a voltage of 100 kV. Each scan consisted in 4000 projections recorded with a continuous rotation around 360° with an exposure time of 0.6 s for each. The total acquisition time was 40 minutes.

3. Results

3.1. Mechanical properties

The tensile stress-strain curves are displayed in Fig. 1-a. It can be seen that the strength levels increase when the grain size is reduced, in good agreement with the literature [5, 7, 54, 55]. Contrarily to most polycrystalline metals, the ductility of this Mg alloy increases with the strength of the sample.

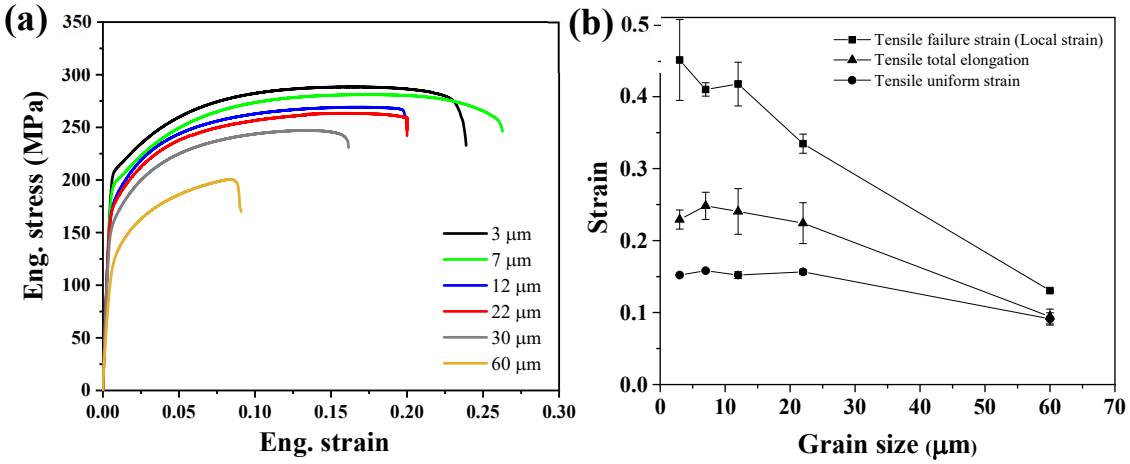

Fig. 1- Mechanical properties of the AZ31 sheet materials with different grain sizes; a) engineering tensile stress-strain curves and b) various measures of tensile ductility as a function of the grain size.

Fig. 1-b plots three different measures of tensile ductility including the tensile failure strain (local strain), the tensile total elongation and the tensile uniform strain, all which increase with reducing grain size. The tensile failure strain is the local strain (principal tensile strain) in the neck area measured at failure (see points 1 and 2 in Fig. 2-a and b). Although the tensile uniform strain shows an increase of 0.045 when grain size reduces from 60 to 3 µm, the grain refinement majorly improves the tensile failure strain such that it shows an overall increase of 0.32 over the grain sizes studied here. Thus, a significant portion of tensile ductility increase occurs in the post-uniform strain region. This is in agreement with previous findings [5]. The strain-hardening exponent (n_{value}) and the plastic anisotropy (r_{value}) remain constant at 0.2±0.01 and 3±0.4, respectively, over the present samples. This also is more-or-less consistent with the literature [5, 54].

3.2. Strain analysis

Fig. 2-a and b show the strain maps for the principle tensile strain determined with DIC at different levels of mean strain measured with the extensometer for the coarse (60 µm) and the fine-grained (3 µm) materials. The stress levels of the strain maps are labelled corresponding to the engineering stress-time curves (Fig. 3). The onset of necking can be determined at the ultimate/peak tensile stress. Fig. 3 shows the evolution of local strain of a point positioned in the gauge region where deformation localizes and ultimately leads to failure. This is compared to the mean strain (solid line). It can be seen that in the coarse-grained material, longitudinal strain is distributed non-uniformly. There is almost no diffuse

necking in the coarse-grained material and the strain localization at a mean strain of 8.7% is clearly inclined in shear to the tensile axis (Fig. 2-a). In the fine-grained material, deformation is more homogenous, suggesting an impact of grain size on deformation heterogeneity at the scale of the specimen in the present case (Fig. 2-b). The post necking deformation in the fine-grained alloy is also higher compared to the coarse-grained counterpart.

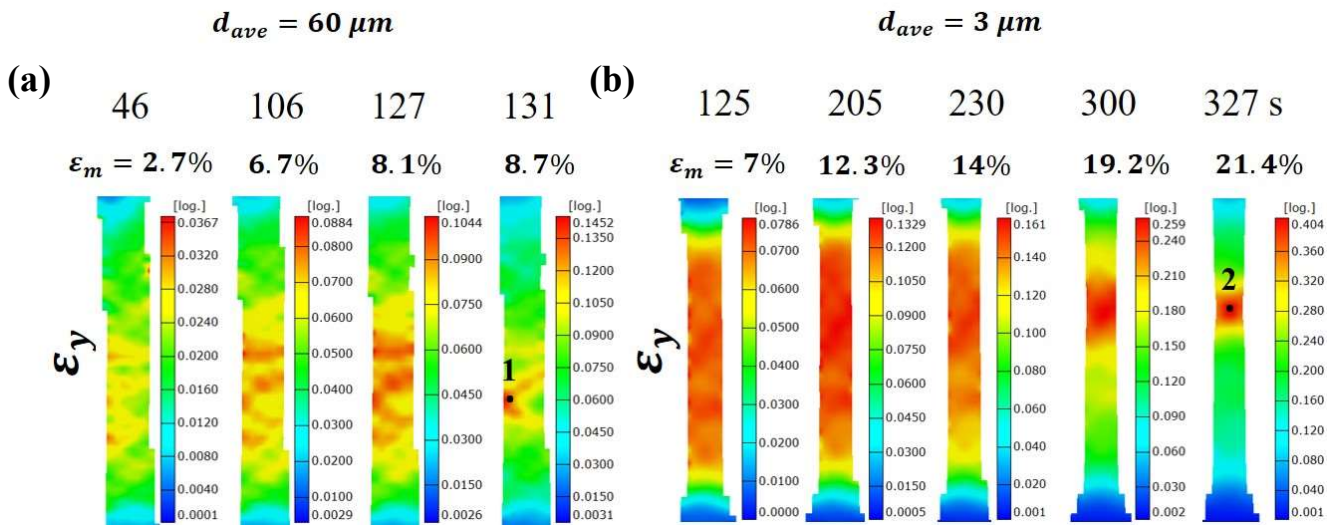

Fig. 2- Strain maps in Y direction of a) the coarse-grained material and b) the fine-grained material during tensile test.

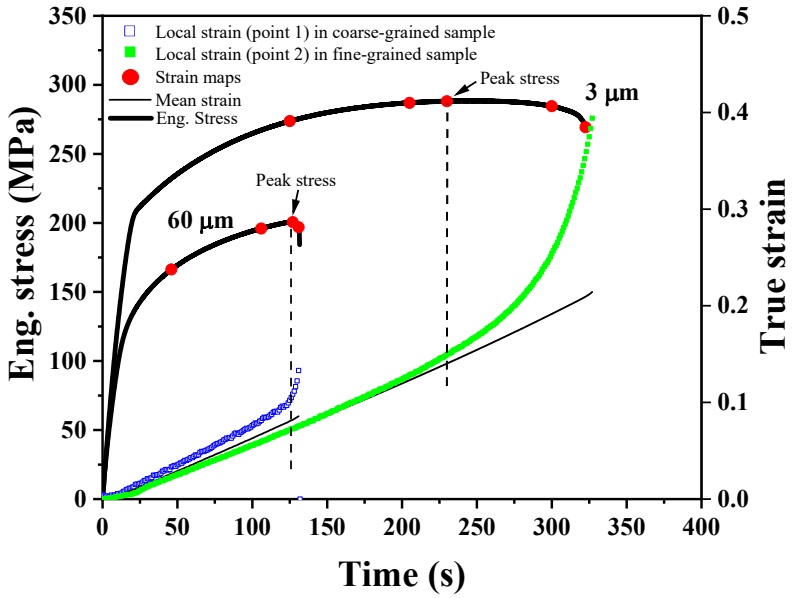

Fig. 3- Engineering stress versus time (red dots corresponding to the strain maps shown in Fig. 2) and local strain as a function of time.

3.3. Damage analysis

3.3.1. Deformed microstructure (twinning)

The deformed microstructure of the materials was evaluated in terms of the fraction of twinned area at different strain levels (Fig. 4) measured with DIC. A point counting technique [28] was employed to examine the twin volume fraction over 1000 grains for each strain level. The twinning activity reduces with grain size reduction (Fig. 5) which is consistent with previous findings [29].

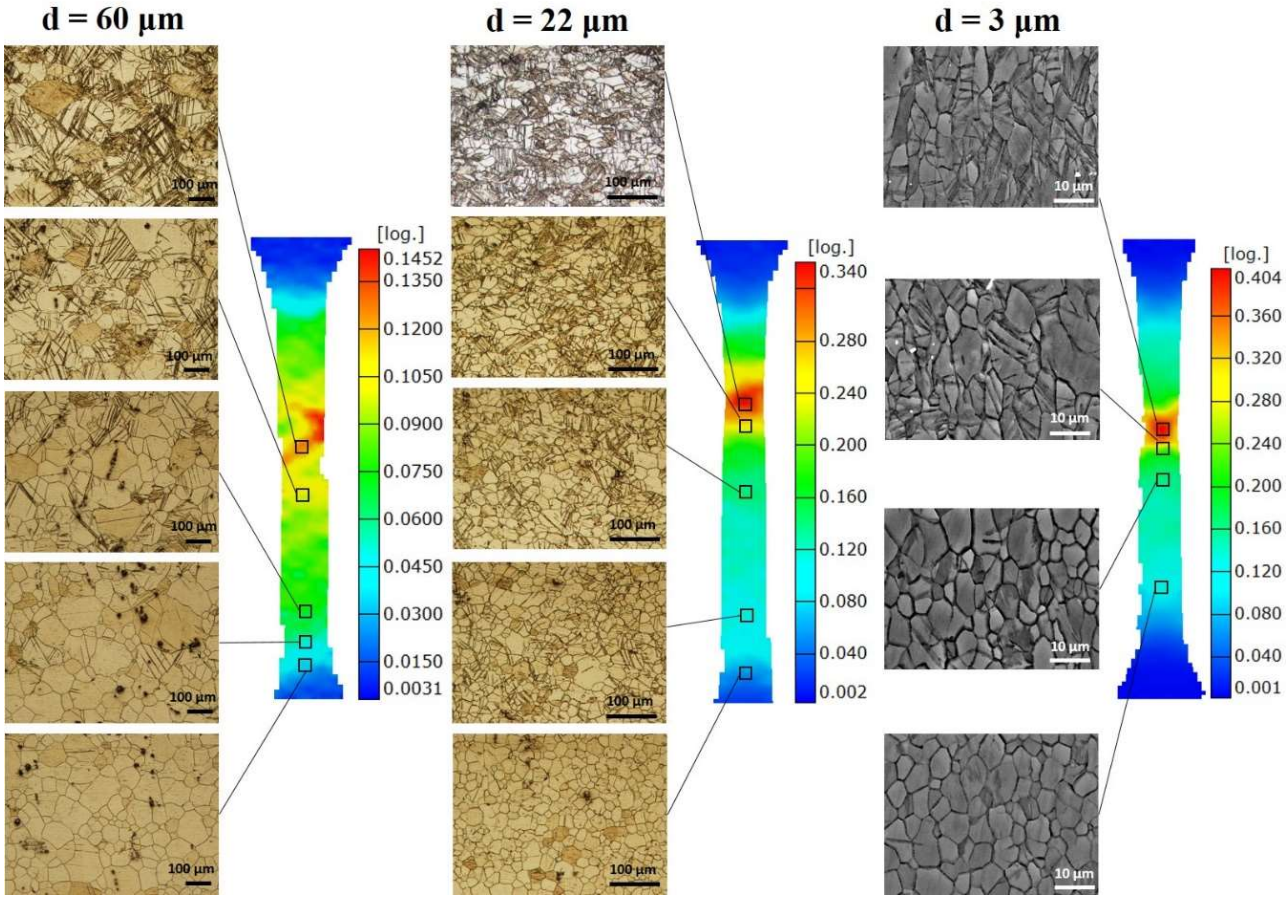

Fig. 4- Deformed microstructure of the materials with grain sizes 60, 22 and 3 µm at different values of strain with the twinned regions and the corresponding strain maps illustrated.

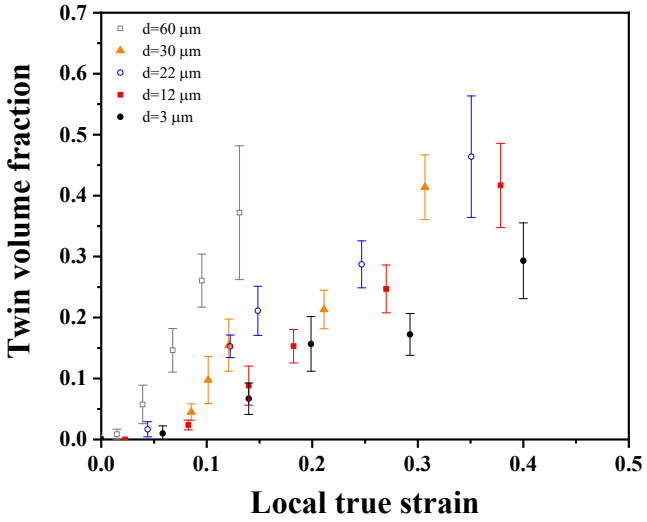

Fig. 5- Twin volume fraction of the deformed materials with different grain sizes versus strain.

At a given strain of 0.14, the fraction of twinned area shows a decrease from approximately 0.38 to nearly 0.06, when grain size reduces from 60 to 3 µm. However, all the materials bar except the finest grained sample display a twin volume fraction at fracture of 0.4 +/-0.05. The twin fraction in the finest grained sample fell at around two thirds of this value.

3.3.2. Void nucleation

Fig. 6 shows the X-ray micrographs in the RD-TD plane close to the mid-thickness of the coarse-grained (60 µm) and the fine-grained (3 µm) samples and their associated 3D models at fracture (RD is the rolling direction). The brighter features in the X-ray micrographs are Mn-rich particles. Two types of voids are detected; type I develops at the second-phase particles (Fig. 6-a and c) and type II forms without obvious contribution from particles (Fig. 6-b and d). The corresponding optical and secondary electron micrographs are provided in supplementary (Fig. S-2). A population of the 50 largest voids in each sample was considered for the statistical analysis (Fig. 7). In the coarse-grained material, almost 50% of the void population nucleated at second-phase particles (type I) and another half of the population nucleated without the contribution of second-phase particles (type II). In the fine-grained material, however, most of the voids (70%) nucleated at second-phase particles (type I). This suggests that the mechanism of void nucleation is sensitive to the grain size and agrees with previous findings [49]. However, there is no correlation between the void size (i.e. void growth) and the void nucleation

mechanisms. Voids with and without second-phase particle contact have similar sizes. This is the case in both the coarse and fine-grained material.

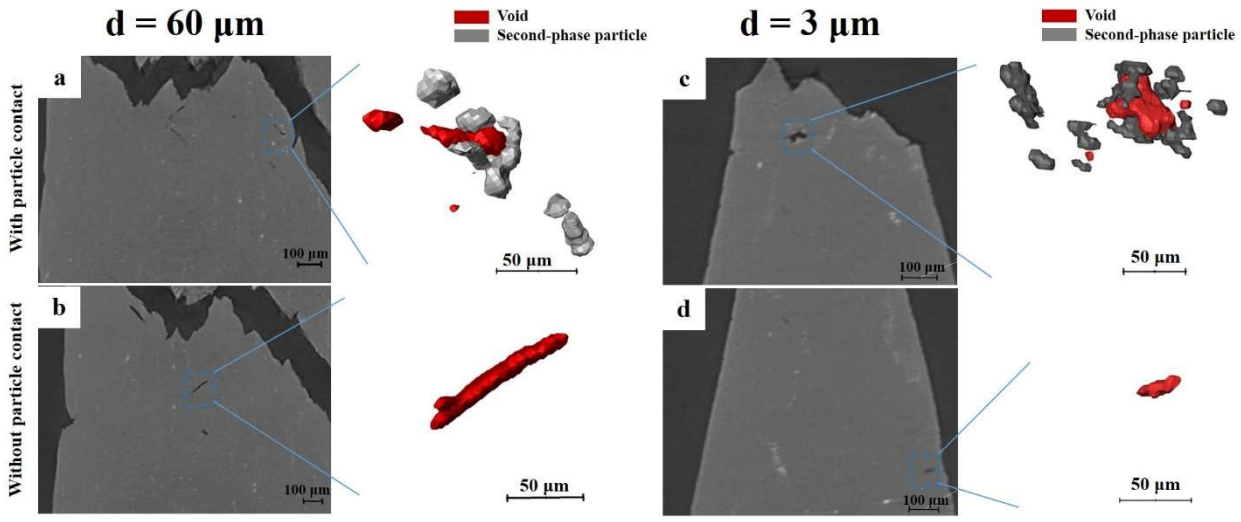

Fig. 6- X-ray micrographs and 3D reconstructed models for the voids nucleated with and without contribution of the second-phase particles in a,b) the coarse and c,d) the fine-grained materials.

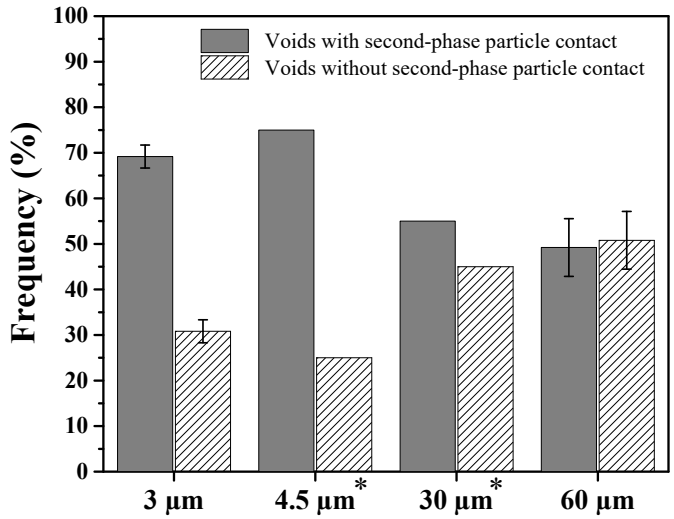

Fig. 7- Frequency of voids with and without second-phase particle contact at failure in the coarse and the fine-grained materials, compared to the samples with grain sizes of 30 and 4.5µm from a previous study (tensile direction was along the RD) [49]*.

Fig. 8-a and b illustrate voids at different intervals of tensile strain in the coarse and fine-grained materials. In both materials void number density is approximately linear with strain (Fig. 9-a). A linear equation (after [33]) was fitted to the data according to the form:

$$N = K'(\varepsilon - \varepsilon_{nucleation}) \qquad \text{Equation 2}$$

where N is the number of voids per cubic millimetre at a given true strain, ε. K' is the apparent rate of void nucleation and and $\varepsilon_{nucleation}$ is the void nucleation strain. There is no significant difference in the rate of void formation with strain between the two grain sizes and so one set of parameters are reported, $\varepsilon_{nucleation}$ and K' are 0.14 and 820+/-91 mm^{-3}.unit $strain^{-1}$. Interestingly, this suggests that the grain size does not markedly influence void nucleation rate (Fig. 9-a).

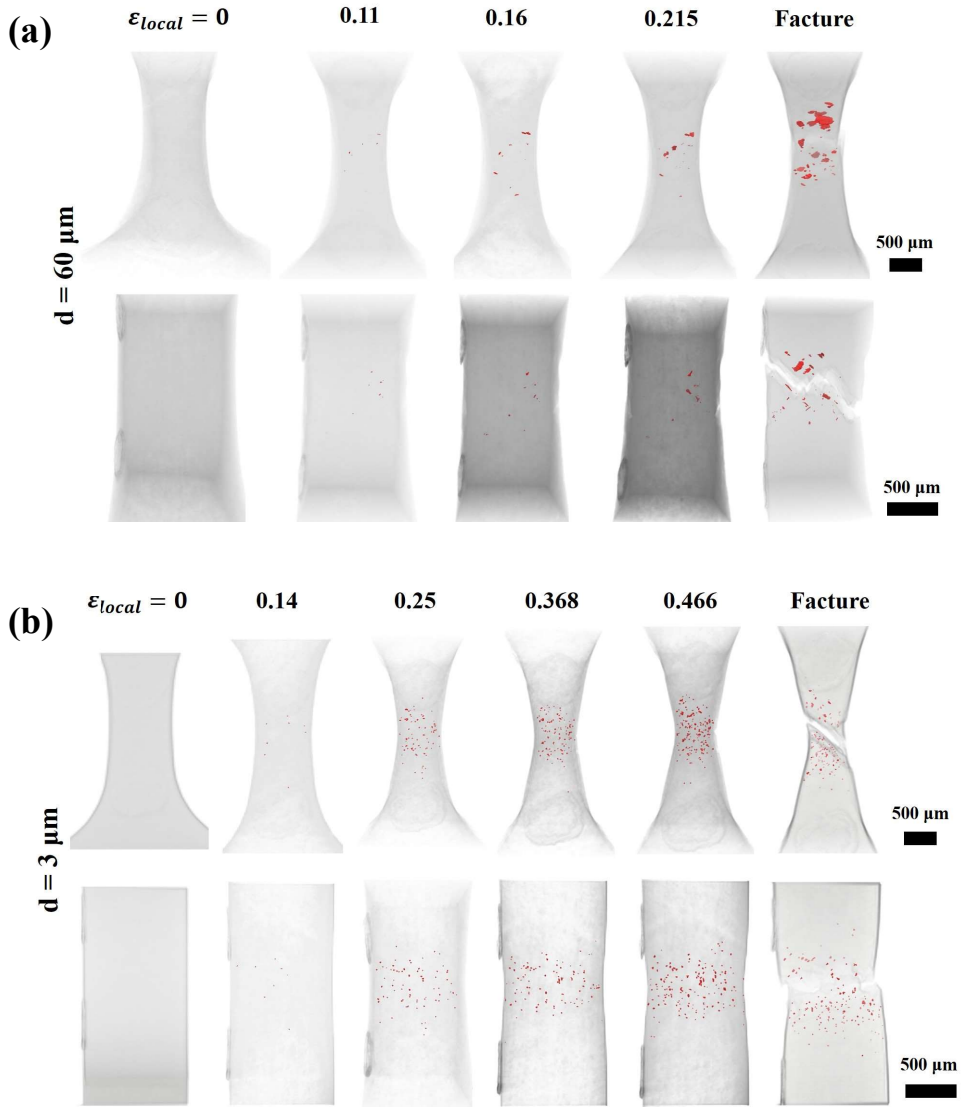

Fig. 8- The 3D reconstructed model showing formed voids at different strain intervals from 'face' and 'side' views in a) the coarse and b) the fine-grained materials.

It should be mentioned that given the current µXCT voxel size of 2.94 µm, the measured void density omits the smaller voids. To obtain some insight into this, samples at fracture were examined employing high-resolution µXCT (1 µm). This led to the detection of a void number density approximately 3 times higher in both the coarse and fine-grained materials. However, the overall effect of grain size is unchanged so the general findings made here are expected to hold for the entire void distribution. The fact that nucleation is measured to be higher with a higher resolution is consistent with what was already observed in [56].

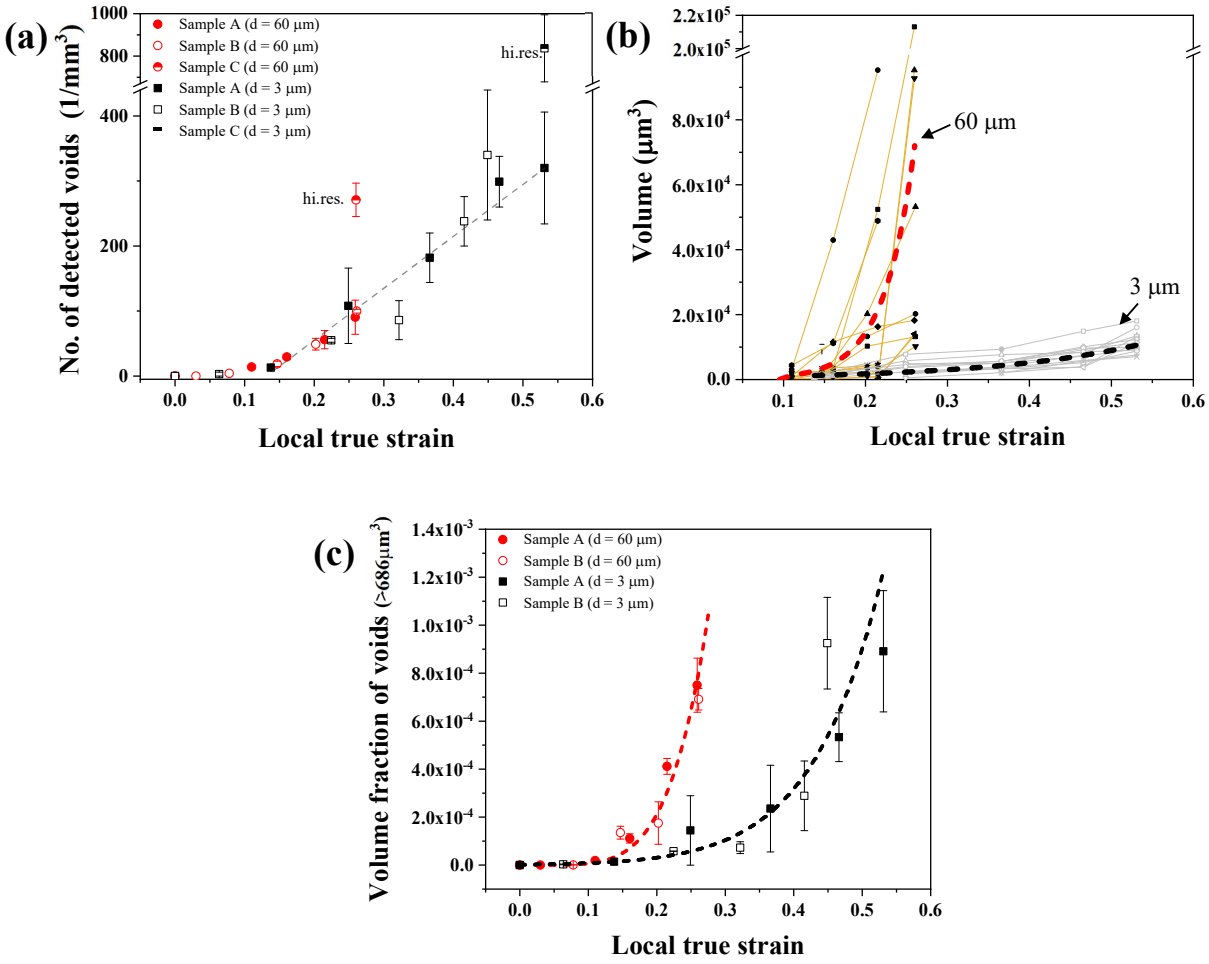

Fig. 9- a) Evolution of void nucleation during tensile loading (hi.res. indicates high-resolution µXCT data), b) the plot of void growth (showing growth of individual voids and the average fitting) and c) evolution of volume fraction of voids during tensile loading in the coarse and fine-grained materials, Y error comes from different maximum grey thresholds (dashed lines shows fitted curves, samples A and B are provided for repeatability of the test and sample C is for high-resolution µXCT).

3.3.3. Void growth

Fig. 9-b shows the evolution with strain of void volume for the 15 largest voids in the coarse and fine-grained materials. These largest cavities can be reasonably assumed to be the same void in each strain step to the next as suggested for instance in [57]. The void growth is clearly considerably more rapid with strain in the coarse-grained material. In the modified Rice and Tracey model [58], it is assumed that voids are spherical in shape. Voids in magnesium alloys, however experience significant shape change during growth (see Fig. 10). Therefore, the equivalent void radius is not a representative measure for void growth. Instead, the modified Pilling and Ridely [59] model used by Nemcko et al. [33] is employed to analyse void growth:

$$V = V_0 exp[\eta(\varepsilon - \varepsilon_{nucleation})] \; for \; \varepsilon \geq \varepsilon_{nucleation} \qquad \text{Equation 3}$$

Here V is the volume of a void at a given true strain, ε. V_0, η and $\varepsilon_{nucleation}$ are the initial volume of a void at nucleation strain, the growth rate parameter and the void nucleation strain, respectively. $\varepsilon_{nucleation}$ of the materials with grain sizes of 60 and 3 µm is 0.14. V_0 (1288 and 1253 mm^3 for the coarse and fine-grained alloys) and η are parameters that give the best least square fit of the void growth model to the experimental results (dashed line curves in Fig. 9-b). This leads to growth rates of $\eta = 22.7$ and $\eta = 5.4$ for the coarse and the fine-grained materials, respectively.

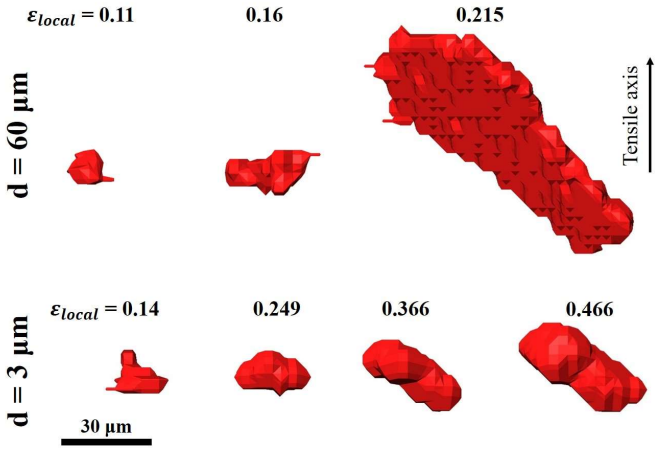

Fig. 10- Growth of a typical void in the coarse and fine-grained materials.

In the fine-grained material, the rate of void fraction development with strain is lower compared to the coarse-grained alloy (Fig. 9-c). This indicates that the fine-grained material is more tolerant to the presence of damage than the coarse-grained counterpart. However, both materials show very similar void volume fractions of ~ 8×10^{-4} at facture. This outcome is in agreement with our previous study [49]. The critical void volume fraction was ~ 6×10^{-4} at fracture in that work and the difference between this value and the present value may be due to the difference in test direction employed. The tensile deformation was along the RD in the previous work.

Fig. 9-c shows the total volume fraction of voids with sizes larger than $686\,\mu m^3$. Fig. 11 shows histograms of size distribution of voids detected in two samples for each the coarse and fine-grained alloys, using the lower-resolution (voxel size = 2.94 µm) and the high-resolution µXCT (voxel size = 1 µm) techniques. There are two categories of voids; voids larger than 686µm^3, V_2, which are analysed by the lower-resolution µXCT and finer voids with $27\,\mu m^3 \leq void\ volume < 686\,\mu m^3$, V_1, which are only analysed by the high-resolution µXCT. While the two samples correspond to different strains, we selected these two conditions for comparison because the total volume fraction of larger voids (void category of V_2) are approximately the same. The total void volume fraction of finer voids (V_1) amounts to ~ 15% of total volume fraction of the larger voids (void category of V_2). Therefore, the finer voids undetected in the present tests are likely to lead to errors in void fraction of this order.

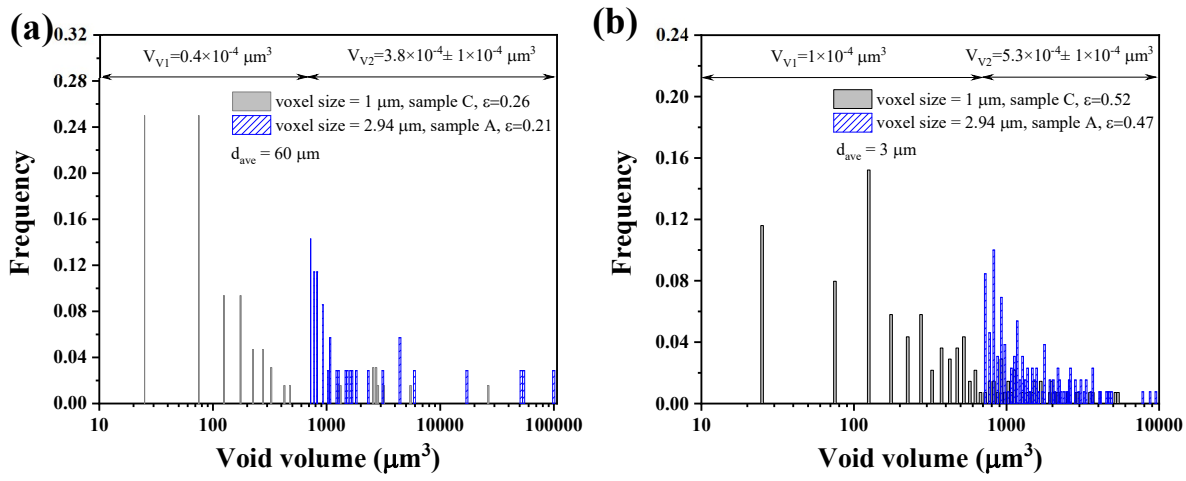

Fig. 11- Histogram of size distribution of voids detected in the coarse (a) and fine-grained (b) samples using µXCT with voxel size of 2.94 and 1 µm (Frequency is related to the number of voids with similar void volume. Total volume fraction of voids in two size categories; $27\,\mu m^3 \leq V_1 < 686\,\mu m^3 \leq V_2$ is included and the two samples for each material has approximately the same V_{V2}).

3.3.4. Void shape

The void shape likely plays a major role in the void linkage and coalescence mechanism. It therefore may influence the failure strain. Fig. 10 and Fig. 12-a illustrate shapes of large voids. In order to analyse the shape, the sphericity and the aspect ratio were calculated. The sphericity was defined by comparing the void surface area to that of a sphere with the same volume as expressed by [33]:

$$\psi = \frac{\pi^{1/3}(6B_v)^{2/3}}{S_v} \qquad \text{Equation 4}$$

Here *Bv* and *Sv* are the volume and the surface area of the object, respectively. The sphericity of a perfect sphere is 1. The aspect ratio is defined by [33]:

$$Aspect\ ratio = \frac{L_{max}}{L_{min}} \qquad \text{Equation 5}$$

where L_{max} and L_{min} are the maximum and the minimum dimensions of a given void, respectively. The shape change of voids with strain is significantly higher in the coarse-grained material, compared to the fine-grained alloy (Fig. 12-b and c).

In the coarse-grained material, a number of large voids show a low sphericity of 0.45 combined with high aspect ratios of 8-11, just before fracture. These are penny shaped voids. In contrast, the voids in the fine-grained materials show higher sphericity and lower aspect ratios of 0.85 and 3-5 respectively.

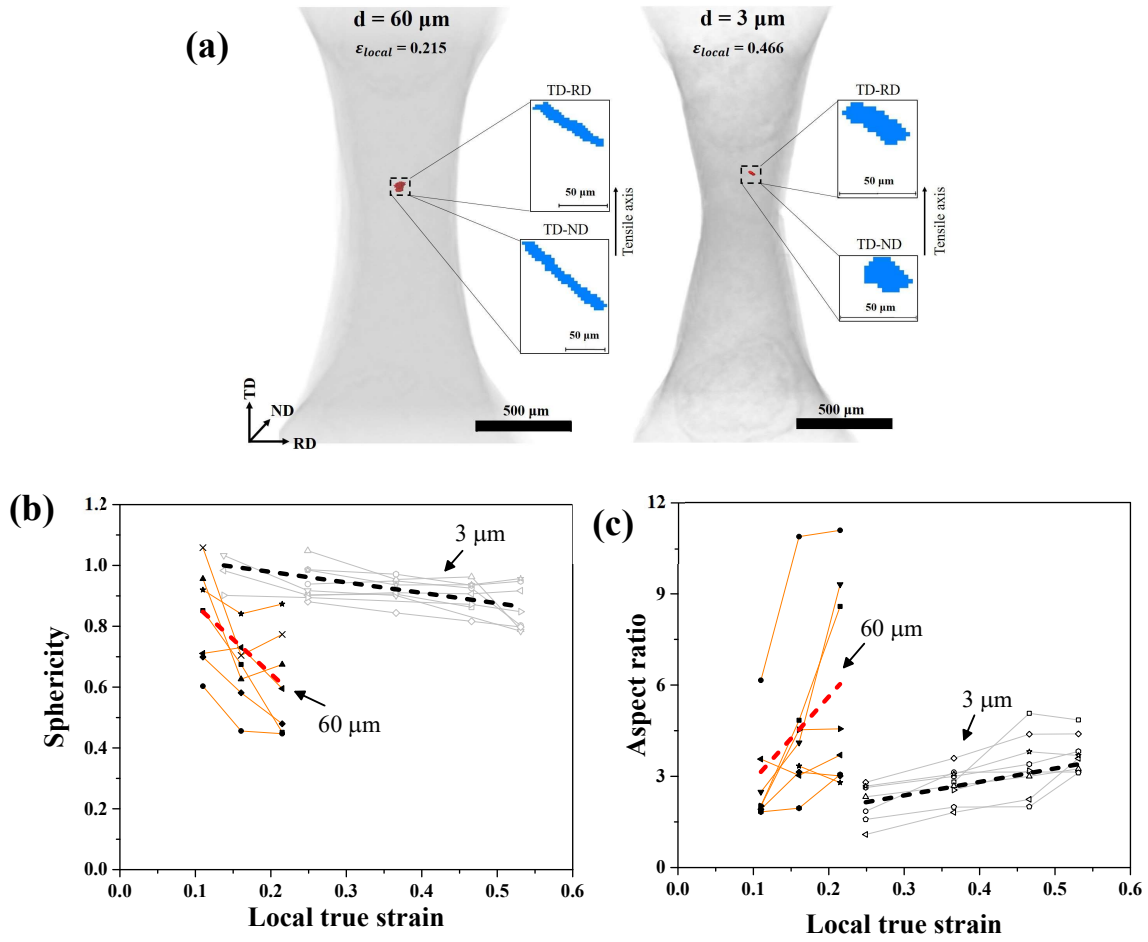

Fig. 12- a) 3D magnified views of a large void at the viewing planes of TD-RD and TD-ND, b) evolution of the sphericity and c) evolution of the aspect ratio of voids formed with strain in the coarse and fine-grained materials (dashed lines show the average trend).

3.3.5. Void coalescence/linkage

The last step of failure involves the linkage and/or coalescence of voids. A drop in the upward trend of the void number density with deformation can indicate significant coalescence of voids into cracks [57, 60]. However, Fig. 9-a shows a monotonically increasing trend for the void number density with strain for both materials which indicates that no significant large scale coalescence occurred (some coalescence may be masked by nucleation of new voids) [60, 61]. This is also evident in the images in Fig. 8. However, 'local' void linkage was observed and an example for the coarse-grained material is given in Fig. 13-a. Growth following void linkage is evident. Fig. 13-b shows an example of void linkage in the fine-grained material. Here the linkage of voids occurred at very high local strains, just before the initiation of fracture. In both cases, the void linkage is likely due to a shear mechanism (i.e. void sheeting) [62]. Fig. 8-a and b also reveal that the final fracture surface in both materials is inclined

to the test direction, which is also consistent with a shear mediated void sheeting type failure mechanism.

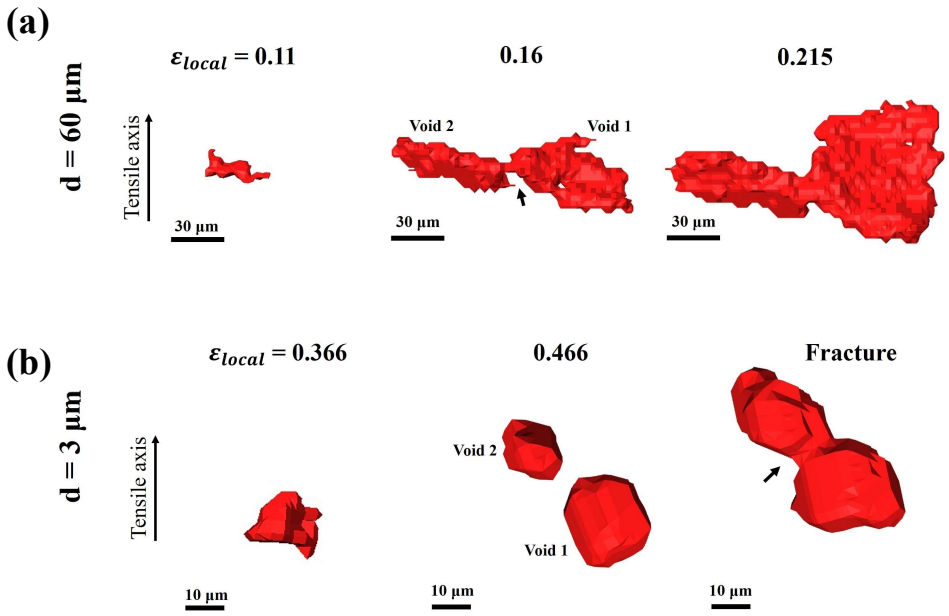

Fig. 13- 3D reconstructed models at different strain values showing void linkage of voids 1 and 2 in a) the coarse-grained material, b) the fine-grained material.

4. Discussion

As noted in the introduction, the rise in tensile ductility seen with grain refinement in magnesium alloys has been associated with a reduction of the twinning activity [28, 29] and the activation of deformation mechanisms such as $\langle c + a \rangle$ non-basal slip [24-26] and grain boundary sliding [10, 11, 27]. The present study reveals that void growth rate is an important part of the picture.

It is interesting that the void nucleation rate appears to be largely insensitive to strain within the present error. This suggests that although there are two main void nucleation mechanisms active - failure at twin/grain boundaries and fracture/delamination at second-phase particles – their activation rate with strain does not differ markedly, once they are active. So, while twinning is suppressed as a contributor to void formation at finer grain sizes, the void formation at second-phase particles provides additional sites and the overall rate of increase in void number density with strain is preserved. It is worth noting that the rate of void nucleation in the studied AZ31 is very similar to that of pure magnesium [33] (i.e. a rate parameter K' in Equation 2 of 743 compared to the present value of 820 mm^{-3}.unit $strain^{-1}$) where

there is no second-phase particles. Importantly, the fine-grained material is able to withstand a far higher number density of voids than the coarse-grained material. The key, it seems, is the void size.

Void growth is seen to depend markedly on grain size. Voids grow more rapidly in coarser grained material. It would thus appear that grain boundaries slow void growth. Void growth within a grain is evidently quite rapid. This may reflect the rapidity of void growth for voids that form within twins, which are often confined to single grains. A void that forms on a grain boundary is also likely to find growth along the highly stressed boundary upon which it formed to be particularly favourable. These findings are reinforced by the lower sphericity of voids in the coarse grained material, suggesting that the large voids formed in these samples formed along planar features such as twins or grain boundary facets. Many voids were seen in both materials with a size matching the grain size, which supports the idea of a period of rapid growth within the grains followed by a period of slower growth once the void size attains to the grain dimension. In the fine grained materials individual void tracking was not able to capture the evolution of voids markedly smaller than the grain size. However, in the coarse grained material a number of the voids that were tracked showed a slower period of void growth following an earlier period of rapid growth (see voids A, B, C and D in Fig. 14) in accord with the present line of reasoning. In any event, it is clear that the rapidity of void growth in the coarse-grained materials leads to a markedly steeper increase in overall void volume fraction with strain compared to the finer grained samples.

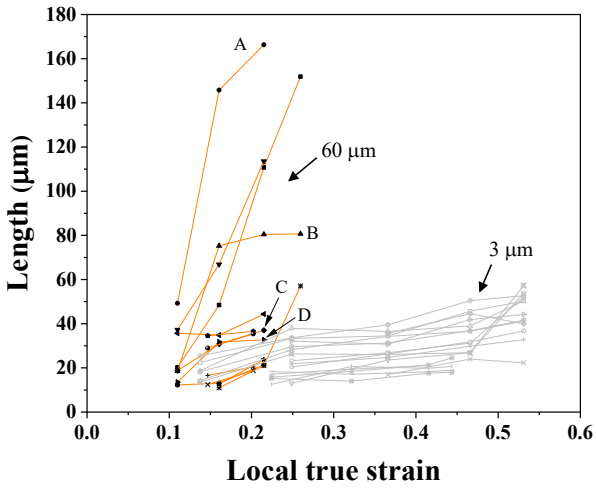

Fig. 14- Evolution of the size (length) of voids formed with strain in the coarse and fine-grained materials (A, B, C, D show voids with early rapid growth followed by a slower period of void growth).

We propose that the effect of grain size on void volume fraction is the dominating relationship. The underlying rationale is that this arises because failure precipitates once a critical void fraction is attained. According to this view, the slower development of void volume fraction with strain in finer grained material - despite higher void number densities - leads to a rise in ductility. To transact this argument, we develop below an expression for failure by void sheeting and show that it predicts failure at a critical void volume fraction. The McClintock model [63, 64] is taken as a starting point and it is thus assumed that the condition for void sheeting is:

$$dP = \tau dA + A d\tau = 0 \qquad \text{Equation 6}$$

Where τ is the shear stress on the shear plane, given by $\tau = k\gamma^n$, γ is the shear strain, A is the load bearing area of the plane, given by $A = (1 - f)A_T$, f is the fraction of voids, approximated here by $f = k''\gamma^a$ (see dashed lines in Fig. 9-c) and A_T is the initial area. Taking the derivatives and substituting gives the following condition for void sheeting:

$$f = \frac{n}{a+n} \qquad \text{Equation 7}$$

Thus it is seen that failure is predicted to occur once the void volume fraction attains to a critical value, set by the terms of the power law exponents that describe the dependencies of stress and void volume fraction on strain. This is consistent with our general observation that failure occurs at a given void volume fraction. In the present work the value seen for a is ~ 5 and that for n is ~ 0.2. This gives a predicted critical void fraction of ~ 4%. The experimental values are much lower, at around 0.1%. Previous work on the notched round samples reported failure at areal void fractions of 0.7% and 1.2% [30]. The high theoretical value for the critical void fraction is most likely a reflection of local strain heterogeneities, which in turn means that the effective local strain exponents differ from the global

values. This can be also inferred from work by Weiler et al. [65], who noted that local areal void fractions near the largest voids were larger than the measured volumetric void fraction.

As noted above, in contrast to other ductile materials such as low carbon steel [66, 67] and certain Al alloys [57, 62, 67], no signs of significant large-scale void coalescence were observed, that is no internal cracking was seen, in the present cases. This is in agreement with previous studies on magnesium alloys [33, 68] and reinforces the interpretation that failure occurs by a void sheeting type mechanism. Although large-scale coalescence occurs in void sheeting it does so in such a rapid manner that it is very difficult to capture in progress during interrupted testing.

5. Conclusion

The present study evaluated the impact of grain size on void formation under tensile loading in magnesium AZ31 alloy using an interrupted *in situ* X-ray microtomography technique. The work leads to the following conclusions:

- It was found that the tensile failure strain increased almost threefold when the grain size was reduced from 60 to 3 μm.
- Grain refinement leads to reduced twins and void volume fractions but does not impact markedly on the relationship between of void number density and strain.
- Grain refinement leads to a greater proportion of voids forming at particles but, because of the higher strain to failure and the relatively unchanged rate of void formation, the finer grained samples displayed higher void number densities at failure.
- Grain refinement leads to a markedly slower rate of void growth.
- Failure appears to be via a void sheeting like mechanism, which is triggered once a critical void volume fraction is attained. The lower rates of void growth in finer grained samples thus lead to higher strains to failure.

Acknowledgments

Financial support from Deakin International Postgraduate Scholarship is gratefully acknowledged. Authors also acknowledge the support from the Deakin Advanced Characterization Facility. S.H.M.A. thanks Prof. Bevis Hutchinson for productive discussions.

Conflict of Interest

The authors declare that they have no conflict of interest.

References

[1] F. Zarandi, S. Yue, Magnesium Sheet; Challenges and Opportunities, INTECH Open Access Publisher2011.
[2] S.R. Agnew, 2 - Deformation mechanisms of magnesium alloys, in: C. Bettles, M. Barnett (Eds.), Advances in Wrought Magnesium Alloys, Woodhead Publishing, 2012, pp. 63-104.
[3] M.R. Barnett, 6 - Forming of magnesium and its alloys, in: M.O. Pekguleryuz, K.U. Kainer, A.A. Kaya (Eds.), Fundamentals of Magnesium Alloy Metallurgy, Woodhead Publishing, 2013, pp. 197-231.
[4] C.M. Cepeda-Jiménez, J.M. Molina-Aldareguia, M.T. Pérez-Prado, Effect of grain size on slip activity in pure magnesium polycrystals, Acta Mater. 84 (2015) 443-456.
[5] D.L. Atwell, M.R. Barnett, W.B. Hutchinson, The effect of initial grain size and temperature on the tensile properties of magnesium alloy AZ31 sheet, Mater. Sci. Eng. A 549 (2012) 1-6.
[6] A. Jain, O. Duygulu, D.W. Brown, C.N. Tomé, S.R. Agnew, Grain size effects on the tensile properties and deformation mechanisms of a magnesium alloy AZ31B sheet, Mater. Sci. Eng. A 486(1–2) (2008) 545-555.
[7] N. Stanford, M.R. Barnett, Fine grained AZ31 produced by conventional thermo-mechanical processing, J. Alloys Compd. 466(1–2) (2008) 182-188.
[8] J.A. del Valle, F. Carreño, O.A. Ruano, Influence of texture and grain size on work hardening and ductility in magnesium-based alloys processed by ECAP and rolling, Acta Mater. 54(16) (2006) 4247-4259.
[9] D. Liu, Z. Liu, E. Wang, Effect of rolling reduction on microstructure, texture, mechanical properties and mechanical anisotropy of AZ31 magnesium alloys, Mater. Sci. Eng. A 612(Supplement C) (2014) 208-213.
[10] H. Somekawa, A. Singh, Superior room temperature ductility of magnesium dilute binary alloy via grain boundary sliding, Scr. Mater. 150 (2018) 26-30.
[11] R.B. Figueiredo, S. Sabbaghianrad, A. Giwa, J.R. Greer, T.G. Langdon, Evidence for exceptional low temperature ductility in polycrystalline magnesium processed by severe plastic deformation, Acta Mater. 122 (2017) 322-331.
[12] N. Stanford, D. Atwell, M.R. Barnett, The effect of Gd on the recrystallisation, texture and deformation behaviour of magnesium-based alloys, Acta Mater. 58(20) (2010) 6773-6783.
[13] R.K. Sabat, A.P. Brahme, R.K. Mishra, K. Inal, S. Suwas, Ductility enhancement in Mg-0.2%Ce alloys, Acta Mater. 161 (2018) 246-257.
[14] K. Hantzsche, J. Bohlen, J. Wendt, K.U. Kainer, S.B. Yi, D. Letzig, Effect of rare earth additions on microstructure and texture development of magnesium alloy sheets, Scr. Mater. 63(7) (2010) 725-730.

[15] J. Bohlen, P. Dobroň, J. Swiostek, D. Letzig, F. Chmelík, P. Lukáč, K.U. Kainer, On the influence of the grain size and solute content on the AE response of magnesium alloys tested in tension and compression, Mater. Sci. Eng. A 462(1) (2007) 302-306.
[16] H. Yu, Y. Xin, M. Wang, Q. Liu, Hall-Petch relationship in Mg alloys: A review, J. Mater. Sci. Technol. 34(2) (2018) 248-256.
[17] W. Yuan, S.K. Panigrahi, J.Q. Su, R.S. Mishra, Influence of grain size and texture on Hall–Petch relationship for a magnesium alloy, Scr. Mater. 65(11) (2011) 994-997.
[18] L. Guo, Z. Chen, L. Gao, Effects of grain size, texture and twinning on mechanical properties and work-hardening behavior of AZ31 magnesium alloys, Mater. Sci. Eng. A 528(29) (2011) 8537-8545.
[19] A. Ghaderi, M.R. Barnett, Sensitivity of deformation twinning to grain size in titanium and magnesium, Acta Mater. 59(20) (2011) 7824-7839.
[20] N. Stanford, M.R. Barnett, Solute strengthening of prismatic slip, basal slip and {101¯2} twinning in Mg and Mg–Zn binary alloys, Int. J. Plast. 47 (2013) 165-181.
[21] H. Yu, C. Li, Y. Xin, A. Chapuis, X. Huang, Q. Liu, The mechanism for the high dependence of the Hall-Petch slope for twinning/slip on texture in Mg alloys, Acta Mater. 128 (2017) 313-326.
[22] H. Somekawa, T. Mukai, Hall–Petch Breakdown in Fine-Grained Pure Magnesium at Low Strain Rates, Metall. Mater. Trans. A 46(2) (2015) 894-902.
[23] H. Somekawa, T. Mukai, Hall–Petch relation for deformation twinning in solid solution magnesium alloys, Mater. Sci. Eng. A 561 (2013) 378-385.
[24] J. Koike, T. Kobayashi, T. Mukai, H. Watanabe, M. Suzuki, K. Maruyama, K. Higashi, The activity of non-basal slip systems and dynamic recovery at room temperature in fine-grained AZ31B magnesium alloys, Acta Mater. 51(7) (2003) 2055-2065.
[25] S. Sandlöbes, S. Zaefferer, I. Schestakow, S. Yi, R. Gonzalez-Martinez, On the role of non-basal deformation mechanisms for the ductility of Mg and Mg–Y alloys, Acta Mater. 59(2) (2011) 429-439.
[26] H. Somekawa, M. Yamaguchi, Y. Osawa, A. Singh, M. Itakura, T. Tsuru, T. Mukai, Material design for magnesium alloys with high deformability, Phil. Mag. 95(8) (2015) 869-885.
[27] H. Somekawa, A. Kinoshita, K. Washio, A. Kato, Enhancement of room temperature stretch formability via grain boundary sliding in magnesium alloy, Mater. Sci. Eng. A 676 (2016) 427-433.
[28] M.R. Barnett, Twinning and the ductility of magnesium alloys: Part II. “Contraction” twins, Mater. Sci. Eng. A 464(1–2) (2007) 8-16.
[29] J. Koike, Enhanced deformation mechanisms by anisotropic plasticity in polycrystalline Mg alloys at room temperature, Metall. Mater. Trans. A 36(7) (2005) 1689-1696.
[30] B. Kondori, T.F. Morgeneyer, L. Helfen, A.A. Benzerga, Void growth and coalescence in a magnesium alloy studied by synchrotron radiation laminography, Acta Mater. 155 (2018) 80-94.
[31] A.K. Ray, D.S. Wilkinson, The effect of microstructure on damage and fracture in AZ31B and ZEK100 magnesium alloys, Mater. Sci. Eng. A 658 (2016) 33-41.
[32] B. Kondori, A.A. Benzerga, Effect of Stress Triaxiality on the Flow and Fracture of Mg Alloy AZ31, Metall. Mater. Trans. A 45(8) (2014) 3292-3307.
[33] M.J. Nemcko, D.S. Wilkinson, On the damage and fracture of commercially pure magnesium using x-ray microtomography, Mater. Sci. Eng. A 676 (2016) 146-155.
[34] J. Kang, D.S. Wilkinson, R.K. Mishra, J.D. Embury, E. Essadiqi, A. Javaid, Microstructural Aspects of Damage and Fracture in AZ31 Sheet Materials, J. Mater. Eng. Perform. 22(5) (2012) 1386-1395.
[35] S. Niknejad, S. Esmaeili, N.Y. Zhou, The role of double twinning on transgranular fracture in magnesium AZ61 in a localized stress field, Acta Mater. 102 (2016) 1-16.
[36] D. Ando, J. Koike, Y. Sutou, The role of deformation twinning in the fracture behavior and mechanism of basal textured magnesium alloys, Mater. Sci. Eng. A 600 (2014) 145-152.
[37] G. Martin, C.W. Sinclair, W.J. Poole, H. Azizi-Alizamini, Local Plastic-Strain Heterogeneities and Their Impact on the Ductility of Mg, JOM 67(8) (2015) 1761-1773.
[38] G. Martin, C.W. Sinclair, R.A. Lebensohn, Microscale plastic strain heterogeneity in slip dominated deformation of magnesium alloy containing rare earth, Mater. Sci. Eng. A 603 (2014) 37-51.

[39] H. Yan, R.S. Chen, E.H. Han, S.W. Xu, S. Kamado, T. Honma, Activation of {1 0 1̄ 2} twinning and slip in high ductile Mg-2.0Zn-0.8Gd rolled sheet with non-basal texture during tensile deformation at room temperature, J. Alloys Compd. 566 (2013) 98-107.
[40] H. Somekawa, K. Nakajima, A. Singh, T. Mukai, Ductile fracture mechanism in fine-grained magnesium alloy, Philos. Mag. Lett. 90(11) (2010) 831-839.
[41] M. Marya, L.G. Hector, R. Verma, W. Tong, Microstructural effects of AZ31 magnesium alloy on its tensile deformation and failure behaviors, Mater. Sci. Eng. A 418(1–2) (2006) 341-356.
[42] M. Lugo, M.A. Tschopp, J.B. Jordon, M.F. Horstemeyer, Microstructure and damage evolution during tensile loading in a wrought magnesium alloy, Scr. Mater. 64(9) (2011) 912-915.
[43] A.K. Rodriguez, G.A. Ayoub, B. Mansoor, A.A. Benzerga, Effect of strain rate and temperature on fracture of magnesium alloy AZ31B, Acta Mater. 112 (2016) 194-208.
[44] M.J. Nemcko, J. Li, D.S. Wilkinson, Effects of void band orientation and crystallographic anisotropy on void growth and coalescence, J. Mech. Phys. Solids 95 (2016) 270-283.
[45] M.J. Nemcko, H. Qiao, P. Wu, D.S. Wilkinson, Effects of void fraction on void growth and linkage in commercially pure magnesium, Acta Mater. 113 (2016) 68-80.
[46] M.J. Nemcko, D.S. Wilkinson, Impact of microstructure on void growth and linkage in pure magnesium, Int. J. Fract. (2016) 1-17.
[47] M.J. Nemcko, D.S. Wilkinson, Investigation of void linkage in magnesium using SEM and micro computed X-ray tomography, 13th International Conference on Fracture 2013, ICF 2013, 2013, pp. 1019-1024.
[48] D. Steglich, T.F. Morgeneyer, Failure of Magnesium Sheets Under Monotonic Loading: 3D Examination of Fracture Mode and Mechanisms, Int. J. Fract. 183(1) (2013) 105-112.
[49] S.H. Mohamadi Azghandi, M. Weiss, B.D. Arhatari, M.R. Barnett, Grain size and void formation in Mg alloy AZ31, J. Alloys Compd. (2019) 152618.
[50] S.H.M. Azghandi, M. Weiss, M.R. Barnett, The Effect of Grain Size on the Bend Forming Limits in AZ31 Mg Alloy, JOM (2020).
[51] A. International, ASTM E112-13 Standard Test Methods for Determining Average Grain Size, West Conshohocken, PA, 2013.
[52] A. International, ASTM B557-15 Standard Test Methods for Tension Testing Wrought and Cast Aluminum- and Magnesium-Alloy Products, West Conshohocken, PA, 2015.
[53] E. Maire, P.J. Withers, Quantitative X-ray tomography, Int. Mater. Rev. 59(1) (2014) 1-43.
[54] A. Jain, O. Duygulu, D.W. Brown, C.N. Tomé, S.R. Agnew, Grain size effects on the tensile properties and deformation mechanisms of a magnesium alloy AZ31B sheet, Mater. Sci. Eng. A 486(1–2) (2008) 545-555.
[55] Q. Miao, L.-x. Hu, H.-f. Sun, E.-d. Wang, Grain refining and property improvement of AZ31 Mg alloy by hot rolling, Trans. Nonferrous Met. Soc. China 19 (2009) 326-330.
[56] C. Landron, E. Maire, J. Adrien, O. Bouaziz, M. Di Michiel, P. Cloetens, H. Suhonen, Resolution effect on the study of ductile damage using synchrotron X-ray tomography, Nucl. Instrum. Methods Phys. Res., Sect. B 284 (2012) 15-18.
[57] E. Maire, S. Zhou, J. Adrien, M. Dimichiel, Damage quantification in aluminium alloys using in situ tensile tests in X-ray tomography, Eng. Fract. Mech. 78(15) (2011) 2679-2690.
[58] L. Lecarme, E. Maire, A. Kumar K.C, C. De Vleeschouwer, L. Jacques, A. Simar, T. Pardoen, Heterogenous void growth revealed by in situ 3-D X-ray microtomography using automatic cavity tracking, Acta Mater. 63 (2014) 130-139.
[59] J. Pilling, N. Ridley, Effect of hydrostatic pressure on cavitation in superplastic aluminium alloys, Acta Metall. 34(4) (1986) 669-679.
[60] C.F. Martin, C. Josserond, L. Salvo, J.J. Blandin, P. Cloetens, E. Boller, Characterisation by X-ray micro-tomography of cavity coalescence during superplastic deformation, Scr. Mater. 42(4) (2000) 375-381.
[61] C. Landron, O. Bouaziz, E. Maire, J. Adrien, Experimental investigation of void coalescence in a dual phase steel using X-ray tomography, Acta Mater. 61(18) (2013) 6821-6829.

[62] A. Pineau, A.A. Benzerga, T. Pardoen, Failure of metals I: Brittle and ductile fracture, Acta Mater. 107 (2016) 424-483.
[63] F.A. McClintock, On the mechanics of fracture from inclusions, ASM, Metals, Park, OH, 1968, pp. 255–277.
[64] F.A. McClintock, S.M. Kaplan, C.A. Berg, Ductile fracture by hole growth in shear bands, Int. J. Fract. Mech. 2(4) (1966) 614-627.
[65] J.P. Weiler, J.T. Wood, R.J. Klassen, E. Maire, R. Berkmortel, G. Wang, Relationship between internal porosity and fracture strength of die-cast magnesium AM60B alloy, Mater. Sci. Eng. A 395(1) (2005) 315-322.
[66] A.A. Benzerga, J. Besson, A. Pineau, Anisotropic ductile fracture: Part I: experiments, Acta Mater. 52(15) (2004) 4623-4638.
[67] J. Besson, Continuum Models of Ductile Fracture: A Review, Int. J. Damage. Mech. 19(1) (2010) 3-52.
[68] B. Kondori, Ductile fracture of magnesium alloys: Characterization and modeling, Texas A&M University, Ann Arbor, 2015, p. 252.